Behavior of nonwoven-geotextile-reinforced sand and mobilization of reinforcement strain under triaxial compression

M. D. Nguyen[1], K. H. Yang[2], S. H. Lee[3], C. S. Wu[4] and M. H. Tsai[5]

[1]*PhD Candidate, Department of Construction Engineering, National Taiwan University of Science and Technology, 43, Sec. 4, Keelung Rd., Taipei 106, Taiwan, Telephone: +886 2-2737-7521, Telefax: +886 2-2737-6606, E-mail: newada119@gmail.com*
[2]*Assistant Professor, Department of Construction Engineering, National Taiwan University of Science and Technology, 43, Sec. 4, Keelung Rd., Taipei 106, Taiwan, Telephone: +886 2-2730-1227, Telefax: +886 2-2737-6606, E-mail: khy@mail.ntust.edu.tw*
[3]*Professor, Department of Construction Engineering, National Taiwan University of Science and Technology, 43, Sec. 4, Keelung Rd., Taipei 106, Taiwan, Telephone: +886 2-2737-6574, Telefax: +886 2-2737-6606, E-mail: leeshh@mail.ntust.edu.tw*
[4]*Professor, Department of Civil Engineering, Tamkang University, 151, Yingzhuan Rd., New Taipei City 251, Taiwan, Telephone: +886 2-2621-5656#2676, Telefax: +886 2-2620-9747, E-mail: cswu@mail.tku.edu.tw*
[5]*Former Master Student, National Taiwan University of Science and Technology, 43, Sec. 4, Keelung Rd., Taipei 106, Taiwan, Telephone: +886 2-2737-7195, Telefax: +886-2-2737-6606 E-mail: roywindforce@hotmail.com*

Received 15 May 2012, revised 29 October 2012, accepted 15 March 2013

ABSTRACT: Laboratory triaxial compression tests were conducted to investigate the stress–strain–volumetric responses of geotextile-reinforced sand and the mobilization and distribution of reinforcement strain/loads and soil–geotextile interface shear stress within reinforced soil. Geotextile-reinforced sand specimens were tested while varying the confining pressures and number of geotextile reinforcement layers. A digital image-processing technique was applied to determine residual tensile strain of the reinforcements after tests and to estimate reinforcement tensile loads. Experimental results indicate that the geotextile reinforcement enhanced peak shear strength and axial strain at failure, and reduced loss of post-peak shear strength. The reinforced specimen had higher shear strength when compared with that of unreinforced soil after deforming by 1–3% of axial strain, which indicates that the geotextile requires a sufficient deformation to mobilize its tensile force to improve the shear strength of reinforced soil. For each reinforcement layer, mobilized tensile strain peaked at the center of the reinforcement and decreased along the radial direction, while the interface shear stress was zero at the center and peaked at a distance of 0.5–07 reinforcement radius from the center. The mobilized tensile strain of reinforcement increases as confining pressure and number of reinforcement layers increase. This work also demonstrates that the strength difference between reinforced and unreinforced soil was strongly correlated with the sum of maximum mobilized tensile forces of all reinforcement layers, indicating that mobilized tensile force of reinforcements directly improved the shear strength of reinforced soil. Last, a number of analytical models to predict peak shear strength of reinforced soil are verified experimentally. This verification demonstrates that mobilized tensile force rather than ultimate tensile strength can be used in analytical models.

KEYWORDS: Geosynthetics, Triaxial test, Geotextile-reinforced sand, Mobilized reinforcement tensile load

REFERENCE: Nguyen, M.D., Yang, K.H., Lee, S.H., Wu, C.S. & Tsai, M.H. (2013). Behavior of nonwoven-geotextile-reinforced sand and mobilization of reinforcement strain under triaxial compression. *Geosynthetics International*, **20**, No. 3, 207–225. [http://dx.doi.org/10.1680/gein.13.00012]

1. INTRODUCTION

Mechanically stabilized earth (MSE) or geosynthetic-reinforced soil (GRS) retaining structures have been widely used in geotechnical engineering projects such as residences, highways, bridge abutments, and slope stabilization. The benefits of MSE retaining structures are good aesthetics, reliability, and low cost. Additionally, easy construction techniques, excellent seismic performance, and a good ability to withstand large deformation without structural distress make MSE structures desirable. Although MSE or GRS structures have many applications, the design of these structures has not been optimized due to the complex interaction between soil and reinforcements.

One approach to investigating soil–geosynthetic interaction treats the soil and the reinforcements as dissimilar materials and tests them using such conventional tests as the pull-out test or soil–geosynthetic interface direct shear test. Parameters obtained from these tests are utilized directly for internal stability designs, as suggested by the current MSE structure guidelines (Elias *et al.* 2001; NCMA 2010). Another approach treats the soil and the reinforcements together as a composite material, and analyzes the stress–strain–volumetric behavior and strength characteristic of reinforced soil. Many studies have been carried out to understand the behavior of reinforced sand using the triaxial compression test (Gray and Al-Refeai 1986; Chandrasekaran *et al.* 1989; Haeri *et al.* 2000; Zhang *et al.* 2006, 2008; Latha and Murthy 2007; Tafreshi and Asakereh 2007; Wu and Hong 2008, 2009), direct shear test (Gray and Ohashi 1983; Athanasopoulos 1993; Farsakh *et al.* 2007), and plane strain test (Boyle and Holtz 1994; Boyle 1995; Hou *et al.* 2011). Test results obtained in previous studies of reinforced sand showed that responses of reinforced sand are influenced by specimen size, confining pressure, and the reinforcement spacing, arrangement, stiffness, strength, and form (i.e., planar layer, discrete fibers, cylindrical, and 3D forms), and the soil–reinforcement interface shear strength. Generally, reinforcements markedly increase peak shear strength and axial strain at failure, and in most cases limit the reduction in loss of post-peak shear strength. Differing from unreinforced specimens that fail along a planar shear plane (i.e., at the angle of $45° + \phi'/2$, where ϕ' is the effective friction angle of soil), reinforced specimens fail via bugling between two adjacent reinforcement layers. Post-failure inspection of dismantled samples showed that the reinforcements experienced tensile deformation. The failure envelopes, defined by the Mohr–Coulomb theory, of both reinforced and unreinforced sand are parallel and, thus, have the same angle of internal shearing resistance. This additional strength by reinforcements can be expressed as an apparent anisotropic cohesion (Schlosser and Long 1974; Hausmann 1976; Bathurst and Karpurapu 1993) or an enhanced internal confining pressure (Ingold and Miller 1983; Chandrasekaran *et al.* 1989; Wu and Hong 2008). A number of theoretical and analytical models have been developed based on these two approaches to predict the peak shear strength of reinforced sand.

Several studies are also available for reinforced clay or reinforced marginal soil (Ingold and Miller 1983; Fabian and Foure 1986; Al-Omari *et al.* 1989; Noorzad and Mirmoradi 2010). In addition to all of the factors affecting reinforced sand, behavior of reinforced clay can also be impacted by moisture content, relative compaction, permeability of reinforcement, and drained/untrained loading conditions. Ingold and Miller (1983) found for clay reinforced with permeable reinforcement that the strength of the reinforced soil improved as reinforcement spacing decreased, whereas for clay reinforced with impermeable reinforcement subjected to undrained loading the strength decreased substantially compared to that of an unreinforced sample. Al-Omari *et al.* (1989) conducted a series of consolidated undrained and consolidated drained triaxial tests on geomesh reinforced clay. Their results indicated for undrained loading that the effective failure envelope of reinforced clay was parallel to the unreinforced envelope and yielded an enhanced cohesion intercept; however, the failure envelopes of reinforced clay from drained tests showed a slight improvement in the cohesion but the friction angle was significantly enhanced.

The strength improvement by thin layers of sand sandwiching on both sides of the reinforcement within reinforced clay has also been evaluated (Sridharan *et al.* 1991; Unnikrishnan *et al.* 2002; Abdi *et al.* 2009). Experimental results demonstrated that thin sand layer inclusions could facilitate the dissipation of pore water pressure inside a clay specimen and increase the interface friction between clay and reinforcement, resulting in improvement of the shear strength of reinforced clay. Experimental results also indicated that there was an optimum sand layer thickness. The provision of thicker sand layers (approximately >10 mm) would not lead to further improvement in the performance of the system.

Until now, little attention has focused on the mobilization of reinforcement tensile strain and loads within soil specimens. That is because measuring deformation of reinforcements inside a test apparatus (e.g., a triaxial cell) is difficult. To the best of our knowledge, only Chandrasekaran *et al.* (1989) have discussed the distribution of reinforcement tensile loads by assuming the distribution corresponding to a third-order polynomial curve. However, this information is important and essential to understanding the mobilization and distribution of reinforcement loads and their relationships with the mobilized shear strength of reinforced soil. This information is also useful when estimating the shear stress distribution along the soil–reinforcement interface, and provides evidence for examining many assumptions in analytical models of reinforced soil.

These observations were the inspiration for this study to conduct a series of triaxial compression tests on nonwoven-geotextile-reinforced sand. A digital image-processing technique is applied to determine residual tensile strain of reinforcements after tests and to estimate reinforcement tensile loads. In addition to stress–strain–volumetric responses of reinforced soil as discussed in many studies, the main objective of this work is to investigate the mobilization and distribution of reinforcement loads and

their relationships with the mobilized shear strength of reinforced sand.

2. EXPERIMENTAL PROGRAM

In this work 16 triaxial compression tests were performed with different confining pressures and numbers of geotextile layers. Furthermore, a digital image-processing technique was employed to determine deformation of reinforcement layers after triaxial compression tests.

2.1. Test materials

2.1.1. *Sand*

This study used uniform and clean quartz sand. Figure 1 shows the grain size distribution of the tested sand. The specific gravity, G_s, coefficient of uniformity, C_u, and gradation, C_c, were 2.65, 1.76, and 1.02, respectively. This sand is classified as poorly graded sand (SP) by the Unified Soil Classification System. The minimum and maximum dry unit weights of sand were $\gamma_{d,min} = 14 kN/m^3$ and $\gamma_{d,max} = 16 kN/m^3$, according to ASTM D4253 and ASTM D4254, respectively. All sand specimens were prepared carefully to maintain a target relative density of 70%. At this target density, the effective shear strength parameters were obtained from triaxial compression tests as $c' = 0$ and $\phi' = 38.5°$ and from direct shear test as $c' = 0$ and $\phi' = 38.8°$.

The shear strength properties of the sand–geotextile interface were determined using a modified direct shear box. The top shear box contained soil, and the geotextile was placed on the top of the bottom shear box and mounted to the two sides of the bottom shear box. The measured interface friction angle was $\phi'_a = 35.8°$ within the normal stress range of 20–100 kPa. The efficiency factor (also called the dimensionless soil–geosynthetic interaction coefficient) is $E = \tan \phi'_a / \tan \phi' = 0.92$. High efficiency factors generally characterize the interfaces of nonwoven geotextiles with sand and are due to the sand penetrating into the fibers of the nonwoven geotextiles during the direct shear test.

2.1.2. *Geotextile*

A commercially available nonwoven interfacing geotextile was selected as the reinforcement in this work. This material was selected based on its large plastic deformation, such that residual deformation of the reinforcement could be preserved easily when the applied tensile force to the reinforcement was released after each test. The load–elongation behaviors of the reinforcement were tested by wide-width and biaxial tensile tests in the longitudinal and transverse directions. The wide-width tensile test was performed according to ASTM D4595 (Figure 2a). The biaxial tensile test was performed by pulling the reinforcement in two perpendicular directions simultaneously (i.e., the transverse and longitudinal directions) using two couple grips of the same width – 145 mm (Figure 2b). Because the actual loading rate of the reinforcement in both directions during the triaxial tests was unknown, the same tensile strain rate in both directions was assigned during the biaxial tensile tests.

Figure 3 shows the wide-width and biaxial tensile test results. Table 1 summarizes the reinforcement tensile strength and stiffness properties. The test results indicate that the geotextile is an anisotropic tensile material; the tensile strength and stiffness of the geotextile in the longitudinal direction (i.e., the stronger and stiffer direction) were larger than those in the transverse direction

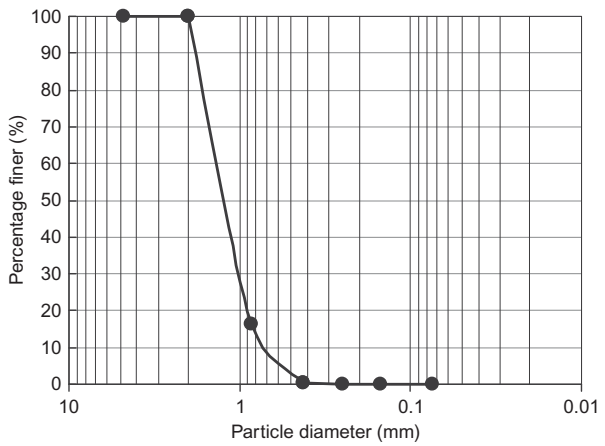

Figure 1. Particle size distribution curve of the tested sand

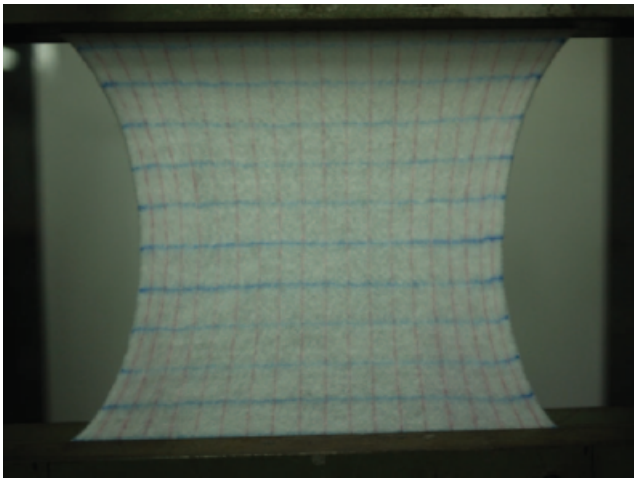

(a)

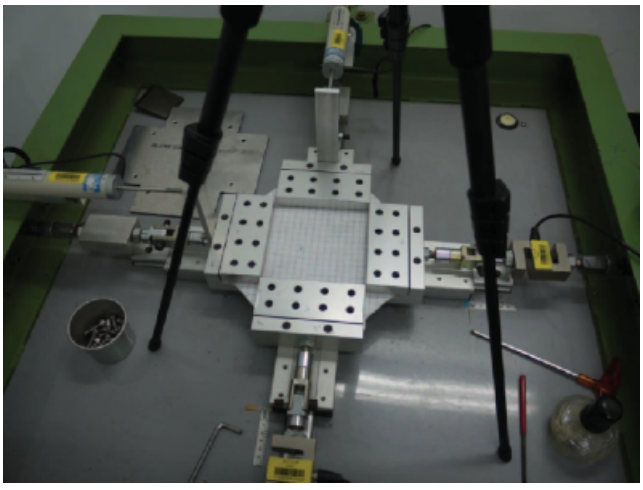

(b)

Figure 2. Photographs of reinforcement tests: (a) wide-width tensile test; (b) biaxial tensile test

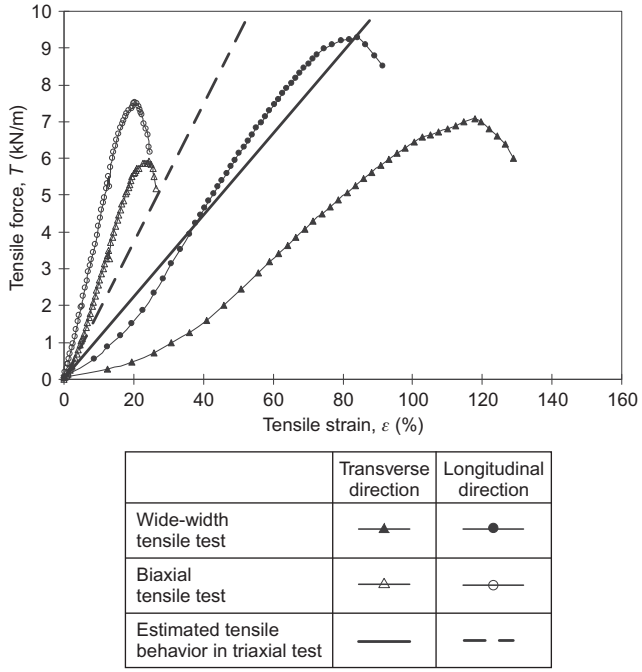

Figure 3. Load–elongation response of geotextile

(i.e., the weaker and softer direction). When compared with uniaxial tensile behavior (i.e., via the wide-width test), the geotextile tested under biaxial loading was stiffer (i.e., high stiffness and mobilized tensile strength at the same strain level). The ultimate tensile strength of geotextile, T_{ult}, under biaxial loading was slightly lower than that under uniaxial loading. This is because stress concentrated easily at the corners of the two perpendicular grips, such that the geotextile broke before it reached its ultimate tensile strength.

To convert measured reinforcement tensile strains to load, the reinforcement load–elongation curve (or stiffness) corresponding to real loading conditions should be properly selected. Walters *et al.* (2002) recommended using in-isolation creep stiffness data to estimate in-situ reinforcement loads from strain measurements for geogrids and woven geotextile. They emphasized that the loading rate can cause significant difference in the estimated stiffness values for reinforcement. The influence of loading rate in this study is believed to be small because the loading rates of the reinforcement in the tensile test (10%/min) and in the triaxial compression test (1–3%/min) are in the same order of magnitude. In additional to the loading rate, the loading type can also influence the load–elongation response of the reinforcement. As shown in Figure 2, the load–elongation responses of reinforcement in the wide-width test differ from those in the biaxial tensile test. Because reinforcement samples within reinforced specimens were loaded axisymmetrically under triaxial compression, the tensile force mobilized in the reinforcement would have differed from the loading conditions in either the wide-width or biaxial tensile test. The real reinforcement loading within reinforced specimens under triaxial compression is likely bounded between uniaxial and biaxial tensile loading conditions. In this study, the load–elongation responses of the geotextile under triaxial compression (the straight lines in Figure 3) were estimated by averaging load–elongation curves from the wide-width and biaxial tensile tests in the same loading direction. This approach is justified later by comparing the observed reinforcement failure strains with the average ultimate strain from the wide-width and biaxial tensile tests. The estimated load–elongation responses from Figure 3 are then utilized to derive reinforcement tensile forces with known reinforcement strain values. To simplify the calculation procedure, we assumed a linear relationship for the estimated load–elongation behavior under triaxial compression: then the values of the estimated reinforcement stiffness, J, in the transverse and longitudinal directions were 15.2 kN/m and 24.4 kN/m, respectively.

2.2. Test procedure

A series of consolidated and drained triaxial compression tests was performed on unreinforced sand and sand reinforced with the geotextile. All test specimens were 50 mm in diameter and 100 mm high. Dry sand was poured into a rubber membrane stretched inside a split mold former and compacted with a small tamper into several layers. The relative density of sand specimens was maintained at around 70%; unit weight was 15.4 kN/m^3. After compaction and leveling of each sand layer, the reinforcement was placed horizontally in the specimen. Figure 4 shows the reinforcement arrangement. After the

Table 1. Physical and mechanical properties of geotextile in the wide-width and biaxial tensile tests

Properties	Values	
Fabrication process	Nonwoven	
Mass (g/m^2)	200	
Thickness, mm	1.78	
Wide-width test	Transverse	Longitudinal
Ultimate tensile strength, T_{ult} (kN/m)	7.08	9.28
Ultimate tensile strain, ε_{ult} (%)	117.8	84.1
Stiffness, J, at ultimate tensile strain (kN/m)	6.0	11.6
Biaxial tensile test	Transverse	Longitudinal
Ultimate tensile strength, T_{ult} (kN/m)	5.91	7.53
Ultimate tensile strain, ε_{ult} (%)	24.3	20.3
Stiffness, J, at ultimate tensile strain (kN/m)	24.3	37.1

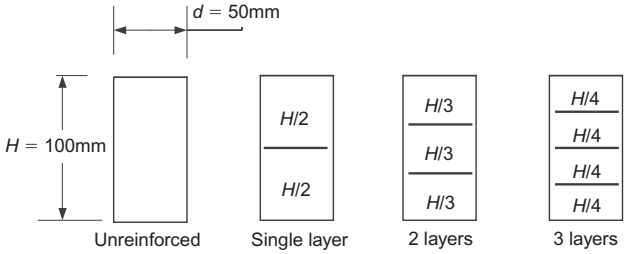

Figure 4. Geotextile arrangement for triaxial compression tests

specimen was prepared, it was placed into a triaxial cell and saturated by allowing de-aired water to flow through the system. A back pressure was applied to facilitate the saturation of soil specimen. The Skempton pore pressure coefficient, B, was checked during the saturation process until the B value was greater than 0.95. Finally, the specimen was consolidated under four confining pressures (20, 50, 100, and 200 kPa) and then loaded axially at a strain rate of 1.5 mm/min. All tests were complete when axial strain of the reinforced soil reached 30%.

2.3. Technique for measuring reinforcement strain

A digital image-processing technique was applied to determine the tensile strain on the reinforcements. Figure 5 illustrates this technique. The reinforcement was first marked with red and blue grid lines with a 10 mm line spacing along the transverse and longitudinal directions, respectively (Figure 5a). A high-resolution digital camera was used to acquire images of the undeformed geotextile before it was embedded in soil. Similarly, the image (at the same resolution density) of the deformed geotextile (Figure 5b) was also acquired after the test when the geotextile was retrieved from the reinforced specimen before further deformation occurred due to changes in the

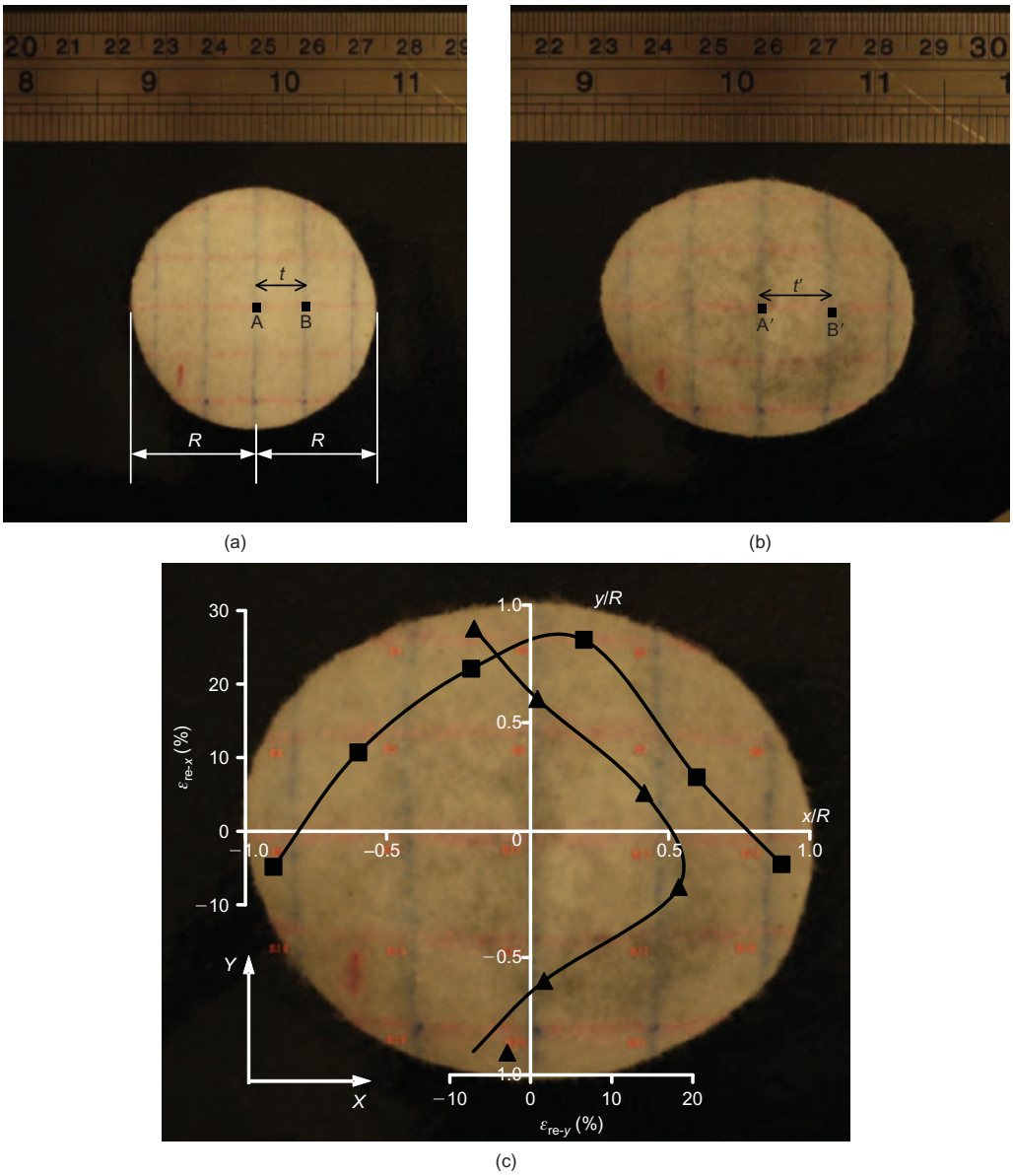

Figure 5. Schematic illustrations of the determination of reinforcement tensile strain: (a) undeformed specimen; (b) deformed specimen; (c) measured residual tensile strains distribution along the *X* axis (transverse direction) and *Y* axis (longitudinal direction)

moisture distribution. The distance between two adjacent nodes along a grid line was determined by counting the number of pixels (i.e., the fundamental unit of a digital image) between adjacent nodes. The strain increment at a segment line was calculated as

$$\varepsilon_{re} = \frac{t' - t}{t} \quad (1)$$

where ε_{re} is the calculated residual tensile strain of a reinforcement, t' is the number of pixels of the deformed reinforcement layer, and t is the number of pixels of the undeformed reinforcement layer. Figure 5c shows an example of the measured tensile strain distribution of a deformed reinforcement specimen in the transverse and longitudinal directions.

Since the deformed reinforcement was retrieved after dismantling the reinforced specimen, tensile force applied on the reinforcement was released; therefore, the test results are representative of residual tensile strain on the reinforcement due to plastic deformation. Because the reinforcement was unloaded, measured residual tensile strain was less than its mobilized tensile strain during testing. Figure 6 shows the relationships between measured residual tensile strain and mobilized tensile strain. The technique for establishing residual and mobilized tensile strain relationships in this work was based on that developed by Leshchinsky *et al.* (2010), who applied a similar technique to estimate reinforcement tensile forces mobilized within a GRS structure from residual tensile strains of exhumed reinforcements. In this study, residual and mobilized tensile strain relationships were established by first testing the reinforcement using the wide-width and biaxial tensile tests at several target tensile strain levels, and then releasing the tensile loadings. Both target tensile strain values (controlled during tests) and the corresponding residual strain values (obtained after releasing the loading) were recorded and plotted (Figure 6). A linear function regressed from relationships between mobilized tensile strain and residual tensile strain was constructed. This function is later used to determine the mobilized tensile strain from measured residual tensile strain.

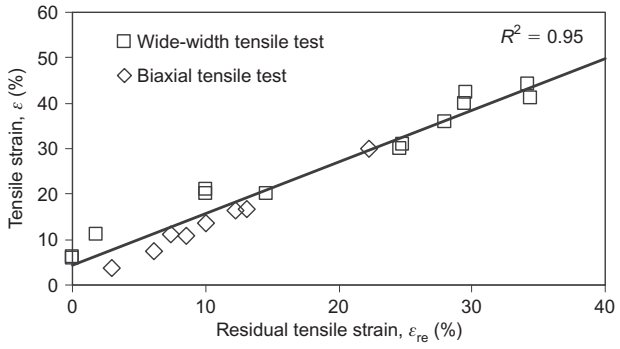

Figure 6. Relationships between the mobilized tensile strain and the residual tensile strain in both transverse and longitudinal directions

3. REINFORCED SOIL BEHAVIOR

3.1. Failure pattern

Figure 7 shows typical images of a reinforced specimen and the deformed geotextile after tests. The reinforced specimen had a ductile behavior that failed when bulging occurred between two adjacent reinforcement layers (Figure 7a). The soil's lateral expansion was restricted by the geotextile layers and a large soil expansion occurred at the middle between two adjacent geotextile layers.

Tensile deformation of reinforcements along the transverse and longitudinal directions was analyzed closely after reinforcements were retrieved from dismantled specimens. Tensile deformation was larger along the transverse direction (lower stiffness) than along the longitudinal direction (Figures 7b to 7d). Geotextile rupture may occur when the number of reinforcement layers or confining pressure is high. The rupture occurred near the middle of the reinforcement, forming a vertical opening perpendicular to the transverse direction (Figure 7c).

3.2. Stress–strain behavior

Figure 8 shows the stress–strain responses of unreinforced and reinforced sand with different numbers of reinforcement layers and different confining pressures. Compared with those of unreinforced specimens, all reinforced specimens exhibited improved stress–strain responses in terms of increases in peak deviatoric stress and axial strain at failure (Figure 8). Moreover, geotextile inclusion reduced the loss of post-peak shear strength. For tests with a large number of reinforcement layers under a low confining

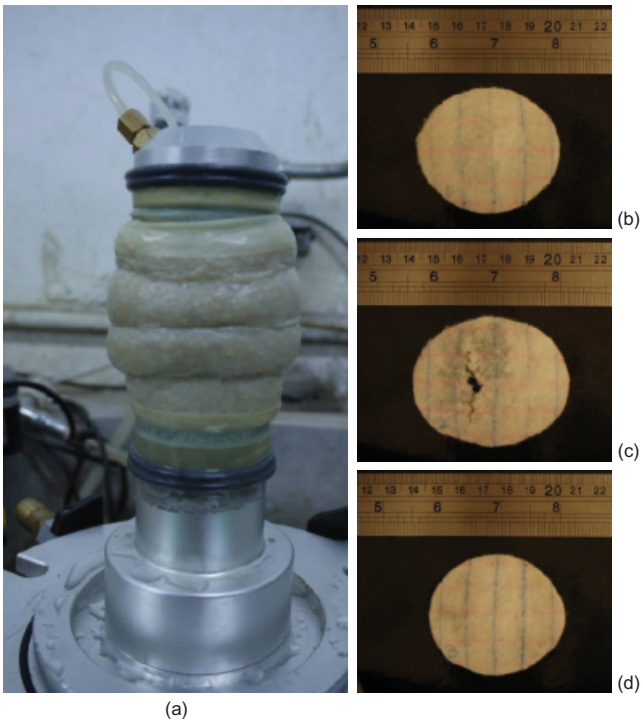

Figure 7. Failure pattern and deformed geotextile: (a) reinforced sand specimen at failure; (b) uppermost layer; (c) middle layer; (d) lowest layer

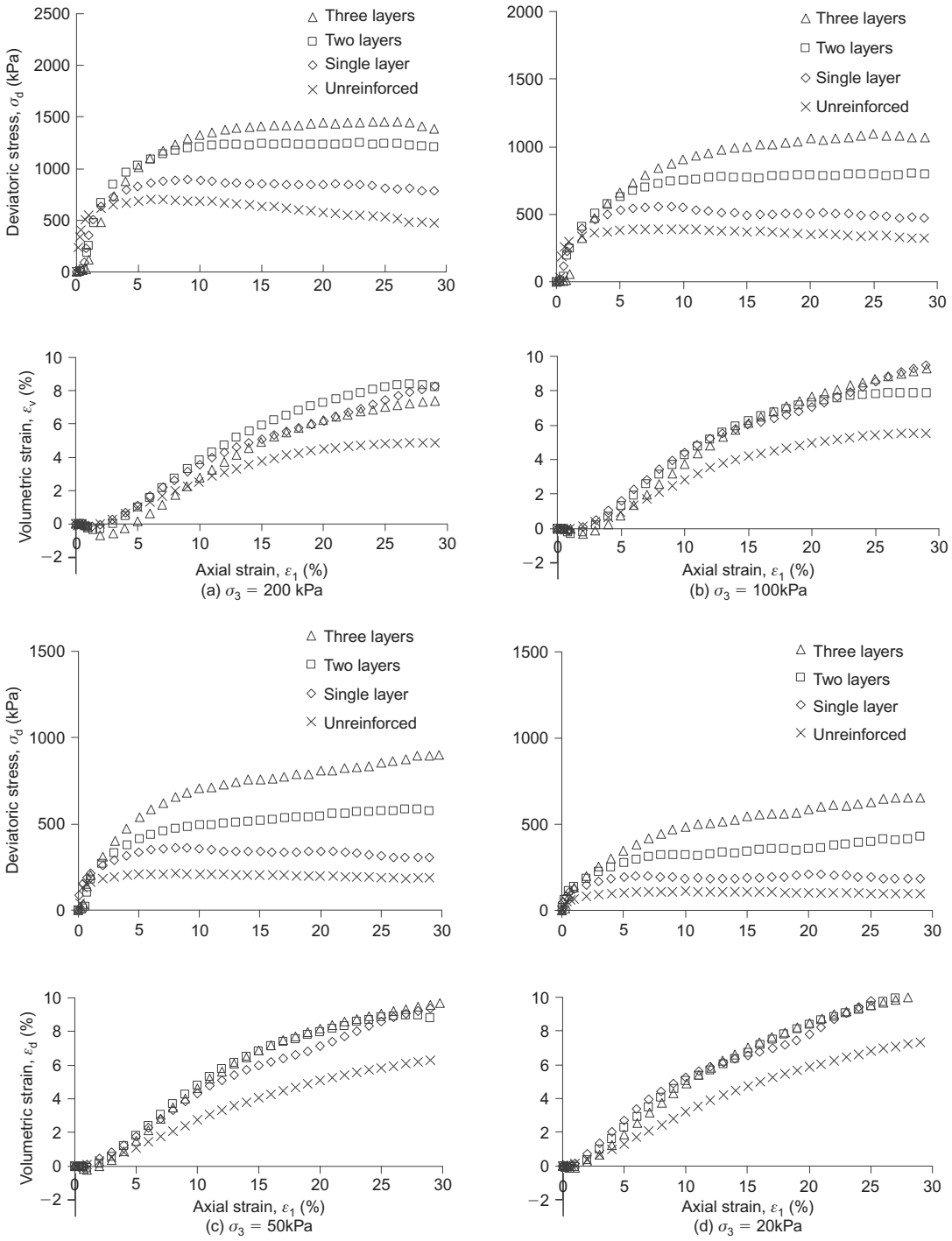

Figure 8. Stress–strain–volumetric responses of unreinforced and reinforced sand with various reinforcement layers and confining pressures: (a) $\sigma_3 = 200$ kPa; (b) $\sigma_3 = 100$ kPa; (c) $\sigma_3 = 50$ kPa; (d) $\sigma_3 = 20$ kPa (the positive sign of volume strain indicates dilatancy)

pressure, shear strength of the reinforced soil continued to increase until the test was completed at 30% of axial strain of reinforced soil.

Overall, geotextile reinforcement enhanced peak shear strength and axial strain at failure, and reduced loss of post-peak shear strength. These effects became increasingly obvious as the number of reinforcement layers increased. The stress–strain behavior was consistent with that in several studies (Haeri *et al.* 2000; Tafreshi and Asakereh 2007; Wu and Hong 2008).

3.3. Volumetric strain

Figure 8 shows variations in volumetric strain against axial strain for both unreinforced and reinforced specimens. The volume of unreinforced and reinforced specimens reduced (i.e., compression) slightly during the initial shearing stage, while the volume of specimens increased (i.e., dilation) as shearing progressed. An increase in confining pressure limits volumetric expansion of both unreinforced and reinforced soil. A comparison of unreinforced and reinforced soil indicates that geotextile inclu-

sion increased compressive volumetric strain during initial shearing and dilatancy during further shearing. However, the effect of the reinforcement layer on volumetric behavior was not clearly shown by test results.

The increase in compressive volumetric strain during initial shearing was likely caused by a decrease in geotextile thickness due to increased axial loading (normal loading to geotextile). The increase in dilatancy of reinforced soil during further shearing was affected by reinforcement stiffness. Notably, Haeri *et al.* (2000) demonstrated that a stiff reinforcement can restrain the dilatancy of reinforced soil. However, this effect was not addressed by this study. Thus, observations discussed in this section only apply to soil reinforced by reinforcements with a similar stiffness.

3.4. Strength ratio and strength difference

The effects of a reinforcement layer and confining pressure in enhancing reinforced soil shear strength are evaluated in this section. Figure 9 shows variations in the strength ratio under different confining pressures and numbers of reinforcement layers. The strength ratio is defined as the ratio of deviatoric stress of reinforced specimens to that of unreinforced specimens under the same axial strain. Generally, the strength ratio increases as axial strain increases, the number of reinforcement layers increases, and confining pressure decreases. Notably, under a range of axial strain of approximately 1–3%, the mobilized shear strength of reinforced soil exceeded that of unreinforced soil. This finding indicates that during initial shearing the geotextile requires a sufficient deformation to mobilize its tensile force to improve the shear strength of reinforced soil. In this range, the reinforced soil required larger deformation (i.e., larger axial strain) to activate the effect of reinforcement for the strength ratio to reach 1.0 when the number of reinforcement layers or confining pressure was increased (see the insert figures in Figure 9).

The effectiveness of reinforcement on improving the shear strength of reinforced specimens was further evaluated using peak strength ratio and strength difference. The peak strength ratio is the peak value of the strength ratio presented in Figure 9. The strength difference $\Delta\sigma_1$ is defined as the difference between shear strength of reinforced soil and that of unreinforced soil under the same confining pressure, which also indicates the net strength improvement by reinforcement. Table 2 summarizes the results and Figure 10 shows the variation of the peak strength ratio with different numbers of reinforcement layers with respect to confining pressure. As the number of reinforcement layers increases, both the strength difference and the peak strength ratio increase.

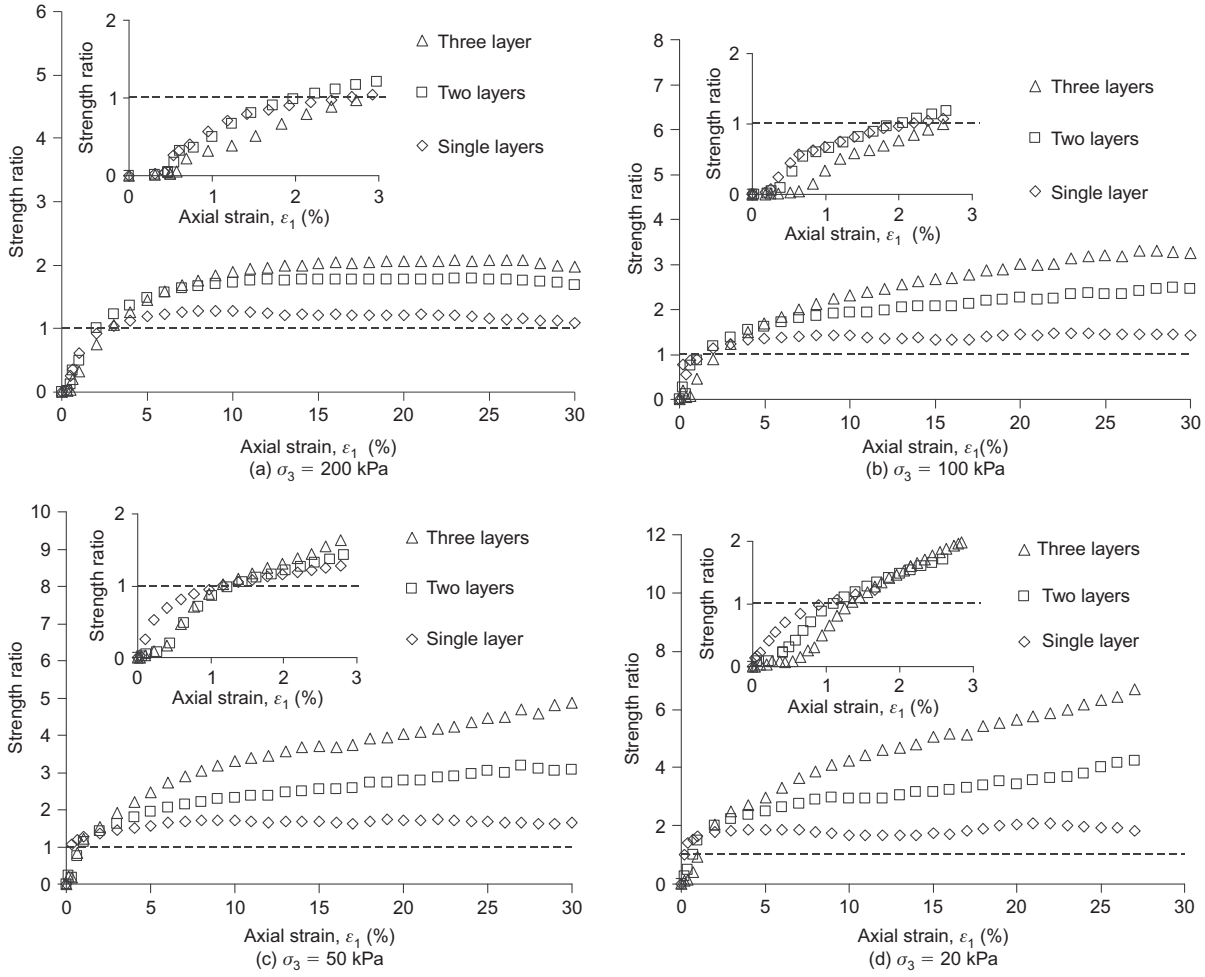

Figure 9. Variation of strength ratio with axial strain. The insert figures correspond to axial strain range from 0% to 3%.

Table 2. Peak strength ratio and strength difference at different confining pressures and numbers of reinforcement layers

Confining pressure, σ_3 (kPa)	Strength difference $\Delta\sigma_1$ (kPa)			Peak strength ratio		
	1 layer	2 layers	3 layers	1 layer	2 layers	3 layers
20	101	329	568	1.84	4.36	6.77
50	149	375	689	1.64	3.07	4.86
100	166	420	704	1.43	2.47	3.25
200	196	553	771	1.58	2.44	2.85

This result indicates increasing improvement of soil shear strength with increasing numbers of reinforcement layers. It also can be observed in Table 2 that, as the confining pressure increases, the strength difference increases but the peak strength ratio decreases. The increasing strength difference suggests that the net strength improvement by reinforcement increases as confining pressure increases due to the mobilization of larger tensile force at higher confining pressure. The mobilization of tensile force with confining pressure will be discussed in next section. The decreasing peak strength ratio with increasing confining pressure indicates that the percentage of the reinforcement's contribution to the overall shear strength of reinforced soil relatively decreases compared with the percentage of soil's contribution (i.e., unreinforced soil) at high confining pressure.

Figure 11 shows that the strength difference declined significantly as reinforcement spacing increased. The strength difference may reduce to zero (extrapolation of the curves in Figure 11 to the horizontal axis) at a certain reinforcement spacing, called the influence spacing of a reinforcement. When reinforcement spacing exceeds the reinforcement influence spacing, the reinforcement does not affect the increase in shear strength of reinforced soil. This work indicated that the influence spacing of reinforcement was in the range of 55–65 mm, which is equivalent to spacing/diameter ratios of 1.1–1.3. This observation corroborates earlier triaxial test results on geotextile-reinforced sand obtained by Gray and Al-Refeai (1986). They concluded that geotextile reinforcements placed at spacing/diameter ratios >1 had little effect on increasing the shear strength of reinforced soil.

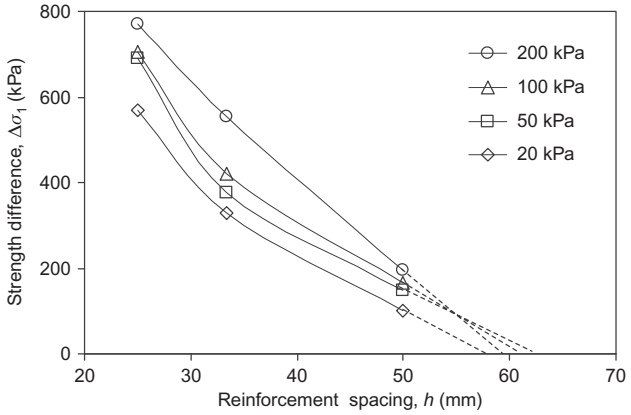

Figure 11. Variation of strength difference with reinforcement spacing

3.5. Failure envelopes

Figure 12 shows the failure envelopes of unreinforced and reinforced sand. The applied vertical stresses at failure, σ_1, increase with confining pressures. The slopes of the failure envelopes of reinforced sand seem to alter at approximately $\sigma_3 = 50$ kPa. The failure envelopes of reinforced sand were parallel to those of unreinforced sand at $\sigma_3 > 50$ kPa. The difference in the friction angle was marginal, resulting in the same angle of internal shearing resistance. The observations of failure envelopes in this

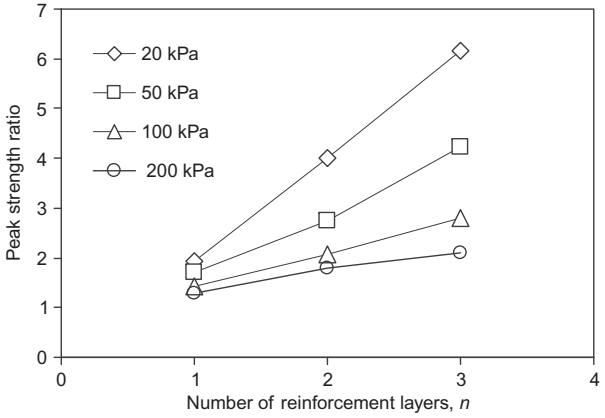

Figure 10. Variation of peak strength ratio with number of reinforcement layers

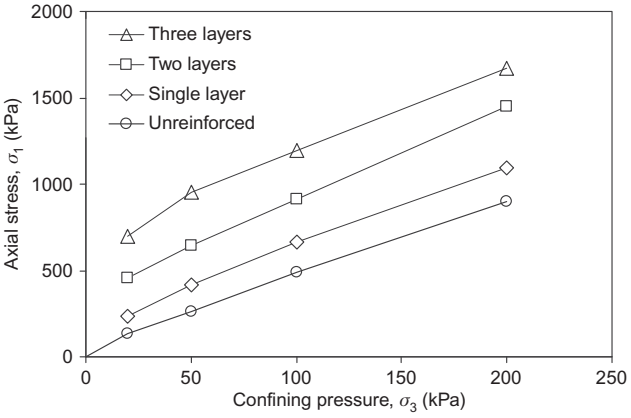

Figure 12. Failure envelopes for unreinforced and reinforced sand

study agree with those for triaxial tests by Long *et al.* (1972), Gray and Al-Refeai (1986) and Haeri *et al.* (2000). They also observed that when the applied confining pressure exceeded a certain threshold (generally in the range of 50–100 kPa), applied vertical stresses at failure of reinforced specimens increased linearly with confining pressures. The increase in reinforced soil shear strength is similar to that of unreinforced soil improved by adding an amount of apparent cohesion.

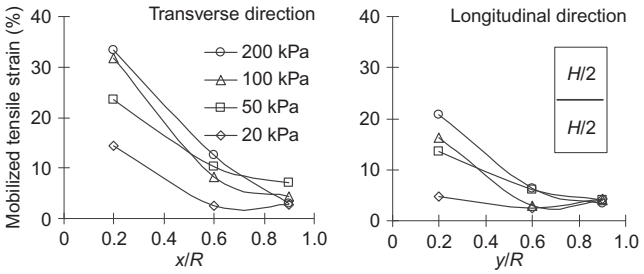

Figure 13. Mobilized tensile strain distribution along the transverse and longitudinal directions of reinforcement; specimens reinforced with single reinforcement layer

4. MOBILIZED REINFORCEMENT TENSILE STRAIN AND FORCE

4.1. Mobilized reinforcement tensile strain

Figures 13–15 present the mobilized reinforcement tensile strain distribution, which was estimated from residual tensile strain as discussed in Section 2.3. Because the strain distribution was approximately symmetrical (Figure 5c), only half of the distribution is shown in the transverse and longitudinal directions. For each reinforcement layer, mobilized tensile strain peaked at the center of the reinforcement and decreased along the radial direction. Some contraction strains (negative values of tensile strain) were observed at the reinforcement's periphery. This is likely caused by the Poisson effect and inhomogeneous deformation on the reinforcement, especially at large-deformation condition. The mobilized tensile strain of the

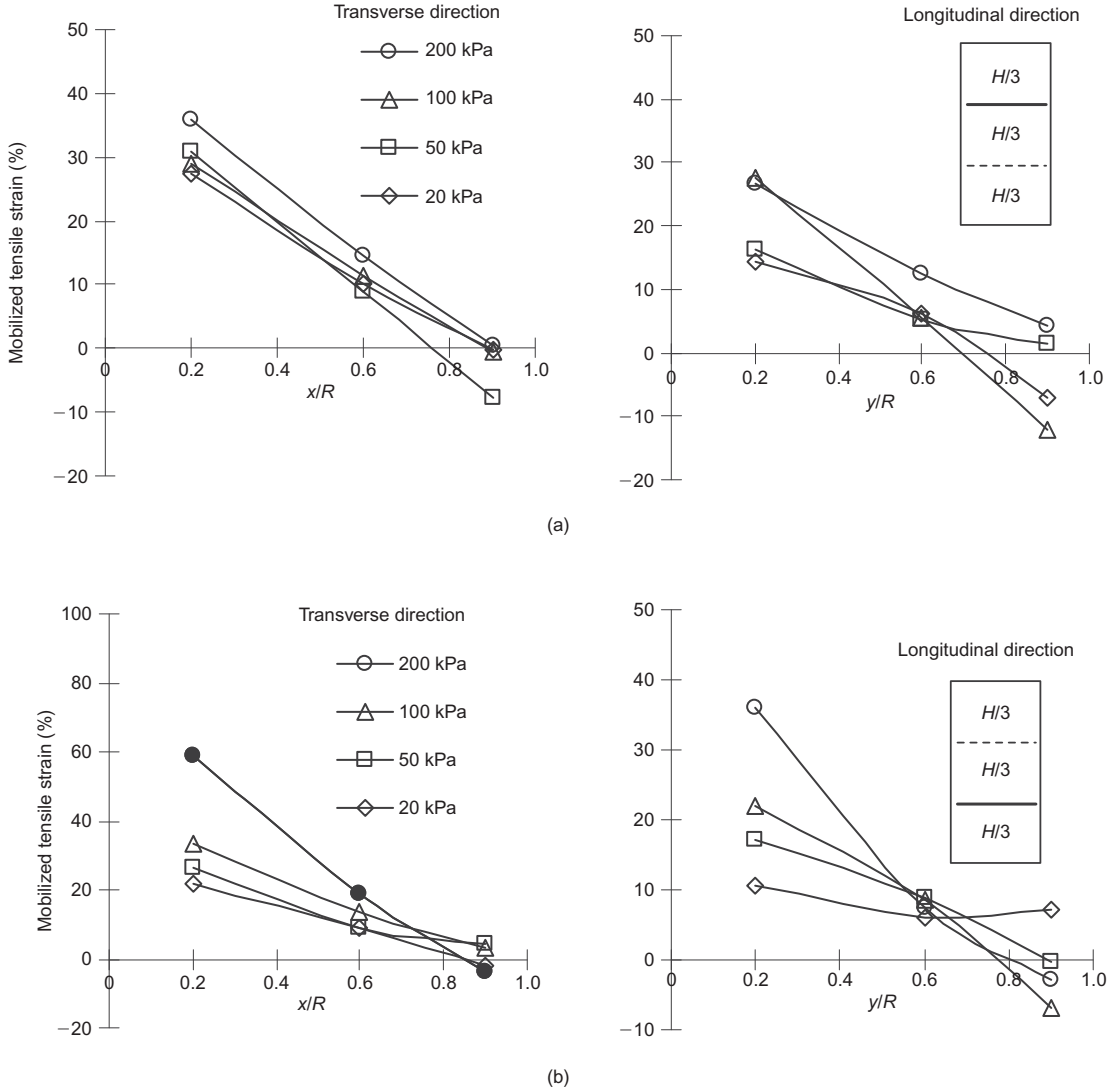

Figure 14. Mobilized tensile strain distribution along the transverse and longitudinal directions of reinforcement; specimens reinforced with two reinforcement layers: (a) upper layer; (b) lower layer. The solid nodes indicate broken reinforcement layers while the blank nodes indicate unbroken ones.

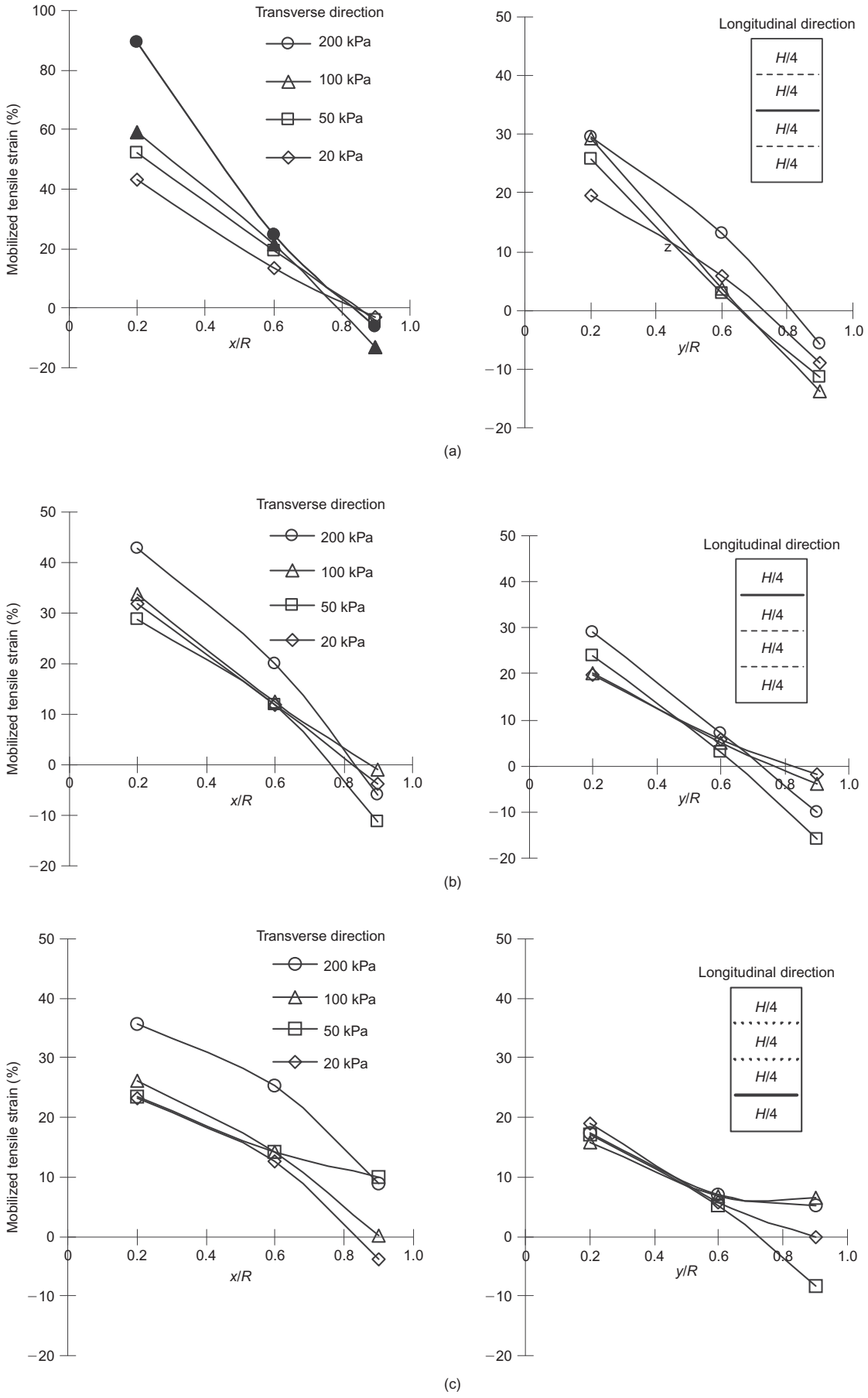

Figure 15. Mobilized tensile strain distribution along the transverse and longitudinal directions of reinforcement; specimens reinforced with three reinforcement layers: (a) middle layer; (b) upper layer; and (c) lower layer. The solid nodes indicate broken reinforcement layers while the blank nodes indicate unbroken ones.

reinforcement was larger in the transverse direction than that in the longitudinal direction. These test results also show that maximum mobilized reinforcement strain increased as the confining pressure and number of reinforcement layers increased (Figure 16). This suggests that the increase in confining pressure and number of reinforcement layers enhanced the soil–reinforcement interaction, resulting in an increase in mobilized tensile strain/force of the reinforcement, further increasing reinforced soil shear strength. A comparison of the effects of reinforcement locations (Figure 15) indicates that mobilized tensile strain increased toward the middle of a specimen and declined toward the top and bottom boundaries of the specimen due to the cap and base restraints (Duncan and Dunlop 1968). This finding demonstrates that in the triaxial cell, nonuniform stress and strain may prevail inside a specimen, and it is unlikely that all reinforcement layers inside a specimen mobilized simultaneously in the triaxial test.

Data points represented with solid black in Figures 14 and 15 represent broken reinforcements that were observed after dismantling reinforced specimens. There were specimens reinforced with two reinforcement layers under 200 kPa, and specimens with three reinforcement layers under 100 kPa and 200 kPa. Figure 7c shows an example of a specimen with a broken reinforcement. Along the reinforcement's transverse direction, the mobilized tensile strains at failure were in the range 60–89%. This range is approximately the average of failure tensile strain from the wide-width tensile test ($\varepsilon_{ult} = 117.8\%$) and failure tensile strain from the biaxial tensile test ($\varepsilon_{ult} = 24.3\%$). This experimental observation supports the preceding assertion that actual reinforcement loading within reinforced specimens is likely bounded between uniaxial and biaxial tensile loading.

4.2. Mobilized reinforcement tensile force

Figure 17 compares maximum mobilized tensile forces of each reinforcement layer in the transverse and longitudinal directions. The mobilized tensile force of reinforcements was estimated by multiplying the mobilized tensile strain (Section 4.1) by the estimated secant stiffness (Section 2.1.2) in the transverse and longitudinal directions. As shown in Figure 17, for each reinforcement layer, maximum mobilized tensile force in the longitudinal direction, $T_{L,max}$, and maximum mobilized tensile force in the transverse direction, $T_{T,max}$, are mobilized equally (all data follow the 1:1 line with $R^2 = 0.90$), except for one data point which was from middle reinforcement layer of a specimen reinforced by three reinforcement layers under a confining pressure of 200 kPa. This reinforcement tensile force value is considered unreasonable because it is much larger than the ultimate tensile strength in the transverse direction measured in the wide-width tensile test ($T_{ult} = 7.08$ kN/m) and biaxial tensile test ($T_{ult} = 5.91$ kN/m). This error may be due to an inaccurate measurement of the residual tensile strain of the broken reinforcement layer when a large opening existed (Figure 7c). The error may also come from estimating the mobilized tensile strain by extrapolating the relationships between the mobilized tensile strain and the residual tensile strain in Figure 6 onto a larger failure tensile strain. Except for this unreasonable data point, the reinforcement was axisymmetrically loaded within reinforced soil in the triaxial compression test (Figure 17). However, due to differences in reinforcement stiffness in the transverse and longitudinal directions, the mobilized tensile strain in two directions differs, as discussed previously. This experimental observation provides solid evidence that supports the assumption of axisymmetric loading of reinforcements in several analytical models for reinforced soil (Chandrasekaran *et al.* 1989; Wu and Hong 2008).

Figure 18 shows the summed maximum mobilized tensile forces from each reinforcement layer within the reinforced soil, $\sum T_{max}$, against the strength difference between unreinforced and reinforced soil, $\Delta\sigma_1$ (i.e., net strength improvement by reinforcement). Since mobilized tensile forces were similar in the two directions, the average of these two forces is used to minimize error from

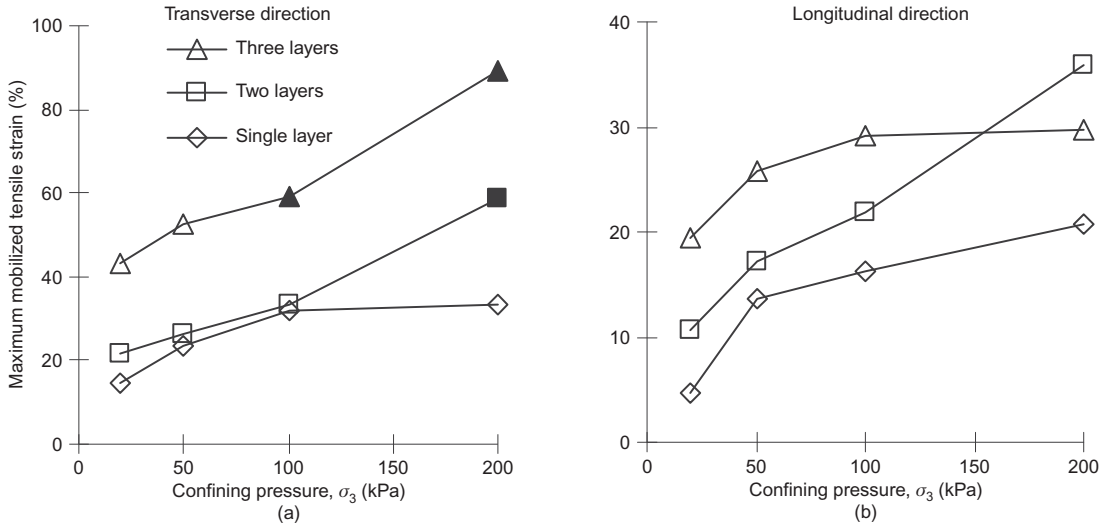

Figure 16. Variation of maximum estimated tensile strain of reinforced specimens with confining pressure: (a) in transverse direction; (b) in longitudinal direction. The solid nodes indicate broken reinforcement layers while the blank nodes indicate unbroken ones.

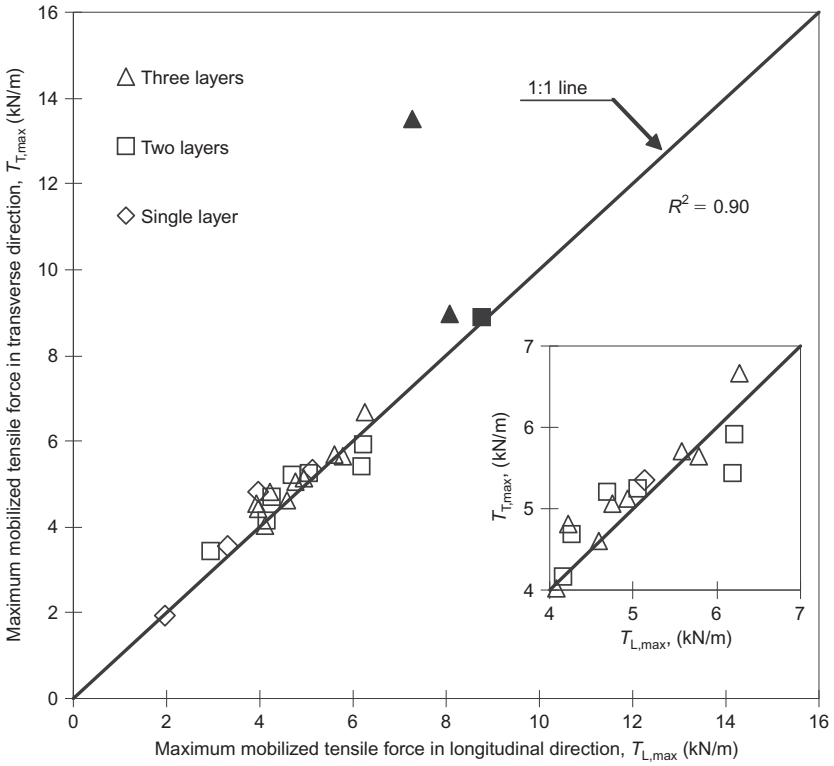

Figure 17. Comparison of maximum mobilized tensile forces in reinforcements in longitudinal and transverse directions. The solid nodes indicate broken reinforcement layers while the blank nodes indicate unbroken ones

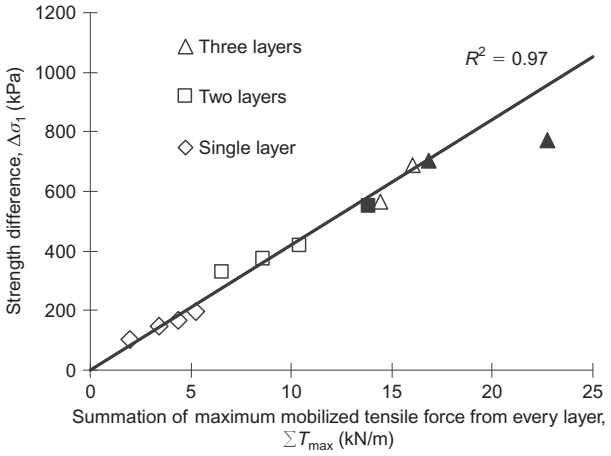

Figure 18. Summation of maximum mobilized tensile forces from every reinforcement layer, $\sum T$ plotted against strength difference, $\Delta\sigma_1$

the measurement and estimation processes. This comparison indicates that the sum of maximum mobilized tensile forces was strongly correlated with strength difference between unreinforced and reinforced soil ($R^2 = 0.97$). This test result demonstrates that the mobilized tensile force of reinforcements directly improves the shear strength of reinforced soil. As $\sum T_{max}$ increased, $\Delta\sigma_1$ increased, resulting in high shear strength of reinforced soil.

4.3. Mobilized interface shear stress

The shear stress distribution, τ, between the soil-geotextile interface can be back-calculated using Equation 2 (Hausmann 1976)

$$\tau = \frac{dT}{2\,dr} \tag{2}$$

where T is the mobilized tensile force in a geotextile, and r is the distance from the center of geotextile discs. In Equation 2, interface shear stress is assumed to act equally on the top and bottom faces of the reinforcements. To obtain a continuous shear stress distribution, a fourth-order polynomial function is first used to fit the estimated tensile force distribution along a reinforcement layer (Figure 19a). The shear stress distribution is then determined with Equation 2 (Figure 19b). Figure 19 shows a typical example of the distribution of mobilized tensile force and interface shear stress along the transverse direction, obtained from the lowest reinforcement layer of a reinforced specimen with three reinforcement layers under a confining pressure of 100 kPa. The shear stress distribution along the longitudinal direction generated a similar result to that along the transverse direction but is not shown here. The mobilized interface shear stress was non-uniform along the transverse direction, and the direction of interface shear stress reversed at the center of the reinforcements (Figure 19b). The interface shear stress was zero at the center of the reinforcements (i.e., $\tau = 0$), peaked at about $x/R = 0.5$–0.7, and then decreased rapidly to about zero near the reinforcement's periphery. The interface shear stress at $r = R$ should theoretically be equal to zero because horizontal stress at this point is a principal stress (i.e., no shear stress existed at the periphery).

Similarly to the interface shear stress distribution in Figure 19b, Figures 20–22 show test results for the interface shear stress distribution in specimens reinforced

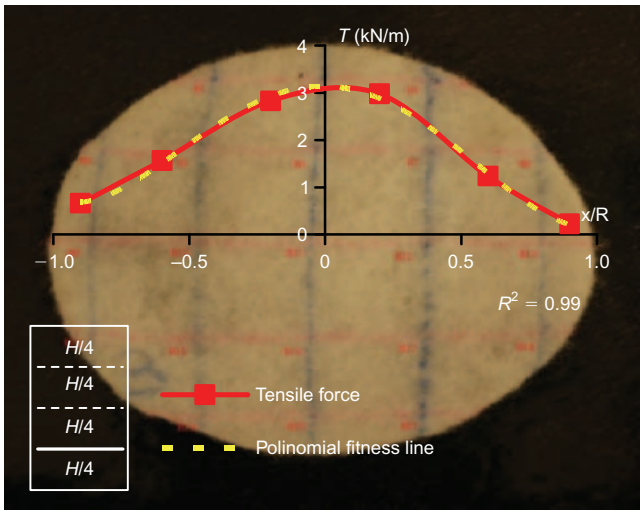

(a)

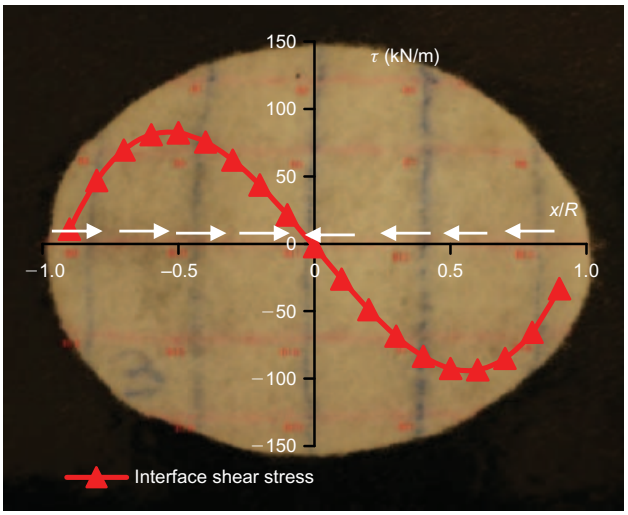

(b)

Figure 19. Distribution of mobilized tensile force and shear stress acting on the lower reinforcement layer of a reinforced specimen with three layers under confining pressure of 100 kPa: (a) tensile force distribution; (b) shear stress distribution

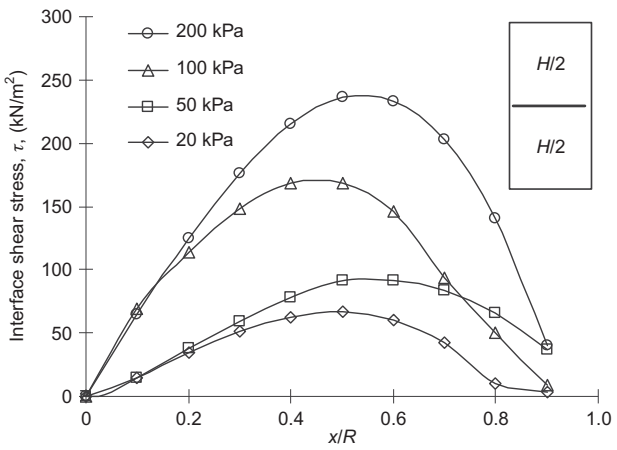

Figure 20. Distribution of shear stress along a reinforcement layer; samples reinforced with a single layer of nonwoven geotextile

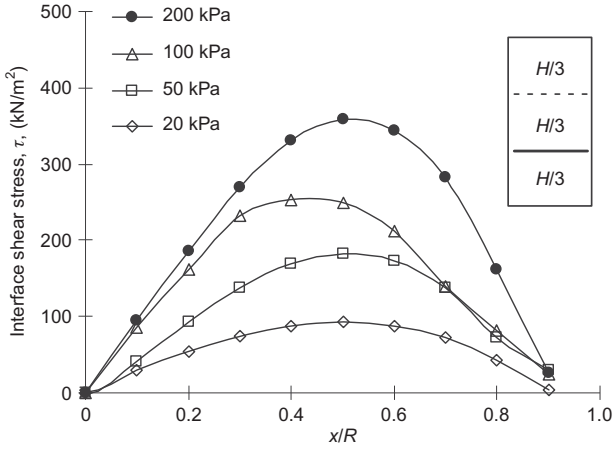

Figure 21. Distribution of shear stress along a reinforcement layer; samples reinforced with two layers of nonwoven geotextile. The solid nodes indicate broken reinforcement layers while the blank nodes indicate unbroken ones

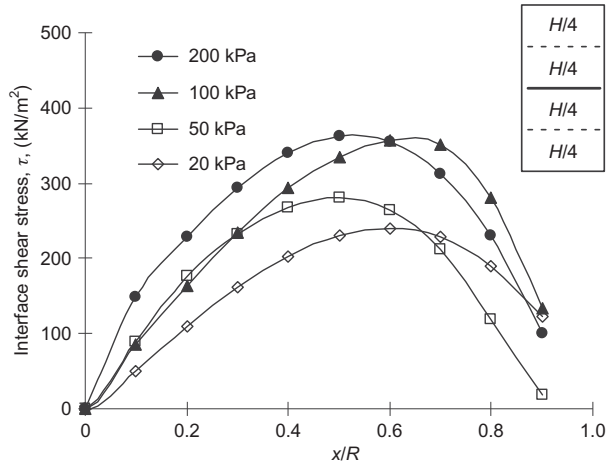

Figure 22. Distribution of shear stress along a reinforcement layer; samples reinforced with three layers of nonwoven geotextile. The solid nodes indicate broken reinforcement layers while the blank nodes indicate unbroken ones

with different numbers of reinforcement layers and confining pressures. The interface shear stress increased as either the confining pressure or the number of reinforcement layers increased. Moreover, the reinforcement layers that broke in the triaxial compression test (solid black symbols in Figures 21 and 22) had similar magnitudes of maximum interface shear (approximately $\tau = 360$ kN/m^2), indicating that a similar magnitude of maximum interface shear stress is required to mobilize fully the ultimate tensile force of reinforcements in triaxial tests.

Ingold and Miller (1983) measured the strain distribution and rotation of principal axes using radiographic techniques. Their results showed that no shear stress existed at the center of reinforcements and that maximum mobilized shear stress occurred close to the reinforcements' periphery. Their observation agrees with the interface shear stress distribution in this study. Additionally, Long *et al.* (1983) and Chandrasekaran *et al.* (1989) also reported a similar trend for the interface shear stress distribution. In their studies, interface shear stress was

zero at the center of reinforcements, and maximum interface shear stress was located at approximately 0.9R. Chandrasekaran *et al.* (1989) further found that the spacing and stiffness of a reinforcement affected mobilized interface friction. The mobilized interface friction increased as reinforcement spacing decreased in their study. However, they claimed that mobilized interface friction was not affected by applied confining pressure, which contradicts test results obtained by this work in which mobilized interface friction increased as confining pressure increased.

5. VERIFICATION OF ANALYTICAL MODELS

Many theoretical and analytical models have been developed to predict the peak shear strength of reinforced soil. These analytical models can be classified into the apparent cohesion approach (Schlosser and Long 1974; Hausmann 1976; Bathurst and Karpurapu 1993) and the additional internal confinement approach (Ingold and Miller 1983; Chandrasekaran *et al.* 1989; Wu and Hong 2008). These two approaches are first reviewed in this section. Prediction results from these analytical methods are then verified against experimental test results presented in this study.

5.1. Apparent cohesion approach

The apparent cohesion approach (Schlosser and Long 1974; Hausmann 1976) considers the increase in shear strength of reinforced soil due to an apparent cohesion c_a generated by the development of reinforcement tensile forces. Therefore, major and minor principal relationships for reinforced soil can be expressed as

$$\sigma'_1 = \sigma'_3 K_p + 2c_a\sqrt{K_p} \tag{3}$$

where K_p is the passive earth pressure coefficient, and c_a is the apparent cohesion due to the development of reinforcement tensile forces. The apparent cohesion, c_a, is conventionally evaluated by limit equilibrium analysis of reinforced soil (Figure 23). In this analysis, in addition to a resistant force, F_R, generated by soil shear strength on the failure plane, a summation of tensile forces, $\sum F_T$, from each reinforcement cut by the failure plane is considered (Figure 23a). The equilibrium equation is

$$\sum F_T + \sigma'_3 A\tan\psi = \sigma'_1 A\tan(\psi - \phi') \tag{4}$$

where ψ is the failure plane angle, and A is the cross-sectional area of the failure plane. The value of $\sum F_T$ is evaluated conventionally using ultimate tensile strength, T_{ult}, for all reinforcement layers, assuming full mobilization of reinforcement tensile strength under the limit state. The value of $\sum F_T$ is then derived as

$$\sum F_T = \frac{A\tan\psi}{h}T_{ult} \tag{5}$$

where h is reinforcement spacing. Combining Equations 3–5 while considering the traditional failure plane angle, $\psi = 45° + \phi'/2$, apparent cohesion can be expressed as

$$c'_a = \frac{T_{ult}}{2h}\sqrt{K_p} \tag{6}$$

The value of T_{ult} in Equation 6 is the average of two transverse tensile strength values obtained from the width-wide tensile test and biaxial tensile test (i.e., $T_{ult} = 6.50$ kN/m). The conventional approach, which uses T_{ult} to predict peak axial stress, σ'_1, of reinforced soil may result in an overprediction when reinforcement tensile strength is not fully mobilized in triaxial tests. To improve prediction accuracy, this study proposes a modified method to predict peak axial stress, σ'_1, of reinforced soil. Differing from the conventional method, which uses ultimate tensile strength, T_{ult}, the proposed modified method uses the maximum mobilized tensile force, T_{max}, as discussed in Section 4.2. As in Figure 23b, resultant tensile force, F_T, for each reinforcement layer is derived as

$$F_T = \int_{-\pi/2}^{\pi/2}(T_{max}\cos\theta)R\mathrm{d}\theta = 2RT_{max} \tag{7}$$

The summation of tensile force $\sum F_T$ is then calculated as

$$\sum F_T = 2R\sum T_{max} \tag{8}$$

where R is the radius of a reinforcement, and $\sum T_{max}$ is the summation of maximum mobilized tensile forces of all reinforcement layers within a reinforced specimen. Then, Equation 8 is combined with Equations 3 and 4 to obtain the modified apparent cohesion, c'_a

$$c'_a = \frac{\sum T_{max}}{\pi R} \tag{9}$$

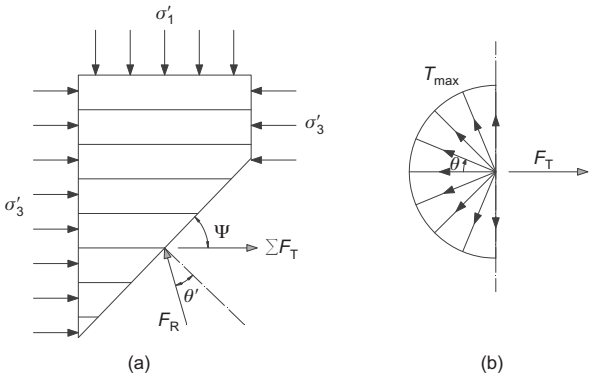

Figure 23. Force analysis in the triaxial compression test of reinforced soil: (a) force diagram; (b) estimation of tensile force F_T

5.2. Additional internal confinement approach

The additional internal confinement approach (Ingold and Miller 1983; Chandrasekaran *et al.* 1989; Wu and Hong 2008) considers the increase in shear strength of reinforced soil due to the additional confining pressure generated by mobilized shear stress along the soil–geotextile interface. Based on this approach, Chandrasekaran *et al.* (1989) applied Equation 10 to estimate maximum total

axial load, P_{max}, on a sand specimen reinforced with circular geosynthetic disks in layers under triaxial loading

$$P_{max} = \pi\sigma_3' \frac{K_{av}}{K_a} \frac{Rh}{\tan(\alpha\phi_a')} \left[\exp\left(\frac{\tan(\alpha\phi')R}{hK_{av}}\right) - 1\right] \quad (10)$$

where K_{av} is the lateral earth pressure coefficient, whose value is the average of Rankine's coefficient of active earth pressure, K_a, and coefficient $K_b = 1/(1+2\tan^2\phi')$, to account for rotation of the principal stress axes within a soil mass between reinforcement layers, and where ϕ_a' is the soil–geotextile interface friction angle, and α is the coefficient, which depends upon the mobilization and distribution of effective friction along the soil–geotextile interface. Peak axial stress, σ_1', is then estimated as

$$\sigma_1' = \frac{P_{max}}{A} \quad (11)$$

In this study, $\phi' = 38.8°$ for unreinforced sand in the triaxial compression test. The value of K_a then becomes 0.23, and K_b can be computed as 0.44. Hence, the K_{av} value was computed as $0.33 = (0.23+0.44)/2$. The angle of interfacial friction, ϕ_a', was 35.8°, which was obtained from direct interface shear tests, as discussed earlier. Based on the back-calculatedα values, Chandrasekaran *et al.* (1989) suggested that $\alpha = 0.65$ for $R/h = 0.5$ and $\alpha = 1.0$ when $R/h \geqslant 1$. Further, Chandrasekaran *et al.* (1989) also demonstrated that the value of α was low for nonwoven geotextiles because of their low stiffness. It should be noted that the prediction of σ_1' using Chandrasekaran's method is sensitive to the assumed value of α, which is difficult to determine precisely, and may limit the accuracy of this method.

5.3. Model verification

Table 3 summarizes measured σ_1' values and prediction results by the three methods. Figure 24 compares measurement and prediction results. The solid line in Figure 24 is the 45° line, representing the degree of equality between measurement and prediction results. The conventional apparent cohesion method overestimated peak axial stress, σ_1', in both unbroken and broken reinforcement cases

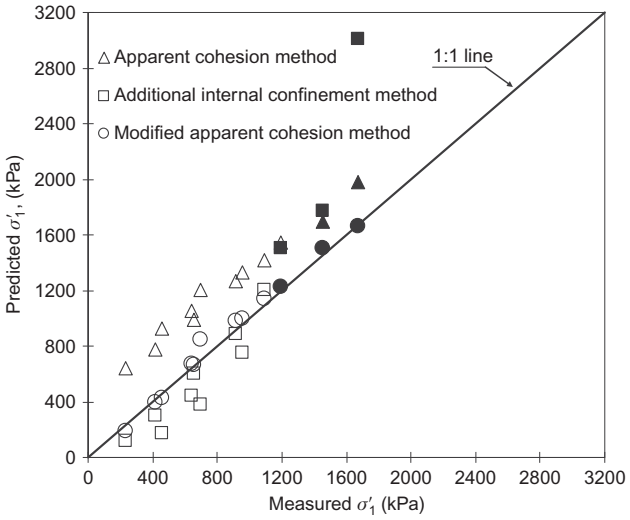

Figure 24. Comparison between experimental and predicted peak axial stress by various prediction methods. The solid nodes indicate broken reinforcement layers while the blank nodes indicate unbroken ones

Table 3. Comparison of peak axial stress observed in experiments for reinforced sand with the values predicted from the three analytical methods

Case	σ_3' (kPa)	Geotextile spacing, h (mm)	Predicted peak axial stress, σ_1' (kPa)			Observed σ_1' from experiment (kPa)
			Apparent cohesion method	Additional internal confinement method	Modified apparent cohesion method	
1 layer; $R/h = 0.5$, $\alpha = 0.65$						
	20	50	644	120	189	231
	50	50	773	301	397	413
	100	50	988	601	662	658
	200	50	1418	1203	1137	1095
2 layers; $R/h = 0.75$, $\alpha = 0.85$						
	240	33	923	177	431	459
	299	33	1052	443	670	639
	358	33	1267	886	979	912
	417	33	1697	1773	1501	1452
3 layers; $R/h = 1$, $\alpha = 1.0$						
	476	25	1202	377	849	698
	535	25	1331	753	995	953
	594	25	1546	1506	1225	1196
	653	25	1975	3012	1665	1670

(Figure 24). Prediction was markedly improved when the modified apparent cohesion method was used. This result confirms the need to use mobilized tensile force instead of ultimate tensile strength in the analytical model. The comparison also implies the mobilized tensile force governs the shear strength of reinforced soil before reinforcement reaches its ultimate tensile strength. Prediction results obtained using the additional internal confinement method, Equation 10, as proposed by Chandrasekaran *et al.* (1989), show that measurement data were underestimated slightly for reinforcement specimens that did not rupture; however, the additional internal confinement method markedly overestimated measurement data for reinforced specimens that rupture. Chandrasekaran *et al.* (1989) also demonstrated that measured axial load capacity for reinforcement specimens with ruptures was overestimated, which was attributed to the sensitivity of prediction results to the assumed α value.

Table 4 presents statistical quantities for model bias values (bias mean μ_b, bias coefficient of variation COV_b, and coefficient of determination R^2) to quantitatively assess the degree of accuracy of the three methods. Bias values are computed as the ratio of predicted axial stress to measured axial stress. A good prediction model yields μ_b and R^2 values that are close to 1, and a COV_b value that is close to zero. A comparison of the three prediction methods indicates that μ_b ($= 1.61$) by the conventional apparent cohesion method and COV_b ($= 0.43$) by the additional internal confinement method have the largest bias. The former indicates that prediction results using the conventional apparent cohesion method overestimated measured values. This is because the conventional apparent cohesion method uses T_{ult} to predict peak axial stress, σ_1', of reinforced soil rather than using actual mobilized values (i.e., T_{max}). The latter suggests that prediction results by the additional internal confinement method have the largest variation, likely due to uncertainties in assuming proper αvalues for various test conditions. A comparison of the three prediction methods (Table 4) demonstrates that the modified apparent cohesion method yields superior prediction results: $\mu_b = 1.02$ and $R^2 = 0.98$ (close to 1) and a $COV_b = 0.09$ (close to zero). These comparison results quantitatively demonstrate that good agreement exists between the measured σ_1' and prediction results by the modified apparent cohesion method.

6. CONCLUSIONS

In this work a series of triaxial compression tests were conducted with sand specimens reinforced with nonwoven geotextile. The main goal of this work is to investigate the mobilization and distribution of reinforcement loads and their relationships with the mobilized shear strength of reinforced soil. Conclusions and discussion points are summarized as follows.

- Geotextile as a reinforcement improves stress–strain performance in terms of increasing peak shear strength and axial strain at failure, and reduces post-peak strength loss. Additionally, geotextile inclusion increases compressive volumetric strain during initial shearing and the dilatancy during further shearing.
- The reinforced specimen has higher shear strength than that of unreinforced soil after deforming by 1–3% of axial strain. This finding indicates that the geotextile requires a sufficient deformation to mobilize its tensile force to improve the shear strength of reinforced soil. The required deformation increases when using additional geotextile layers or applying a high confining pressure.
- The mobilized tensile force peaks at the center of reinforcements and reduces to approximately zero at the reinforcements' periphery. The mobilized reinforcement force increases as the confining pressure and number of reinforcement layers increase. Maximum reinforcement tensile forces in the longitudinal direction, $T_{L,max}$, and in the transverse direction, $T_{T,max}$, are equally mobilized. This result suggests that the reinforcement is axisymmetrically loaded within the reinforced soil under triaxial compression. However, due to the difference in reinforcement stiffness in the transverse and longitudinal directions, reinforcement deformation in the geotextile is anisotropic.
- The value of the strength difference, $\Delta\sigma_1$, increases linearly as the summation of maximum mobilized tensile forces from each layer within a specimen, $\sum T_{max}$, increases. This experimental finding indicates that the mobilized tensile force of the reinforcement improves the shear strength of reinforced soil directly. These test results also demonstrate that the strength difference declines significantly as reinforcement spacing increases. At reinforcement spacing/diameter ratios of 1.1–1.3, the strength difference may reduce to zero and the reinforcement does not influence the increase in reinforced soil shear strength.
- The mobilized shear stresses between the geotextile and sand are distributed non-uniformly in the geotextile layer. The interface shear stress is zero at the center of the reinforcements, gradually increases, peaks at about $x/R = 0.5–0.7$, and then decreases

Table 4. Results of statistical analyses

Method	Parameters			
	Number of data points	Mean, μ_b	COV_b	R^2
Apparent cohesion method	12	1.61	0.29	-0.03
Additional internal confinement method	12	0.91	0.43	0.70
Modified apparent cohesion method	12	1.02	0.09	0.98

rapidly to about zero near the reinforcement's periphery. The interface shear stress increases as either the confining pressure or number of reinforcement layers increases. The broken reinforcement layers have similar magnitudes of maximum interface shear, indicating that a similar magnitude of maximum interface shear stress is required to fully mobilize the ultimate tensile force of reinforcements in triaxial tests.

- The verification of analytical methods demonstrates that the proposed modified method using mobilized tensile force, T_{max}, predicts peak axial stress of reinforced soil accurately.

Finally, it should be remembered that the data presented relate to laboratory tests carried out on saturated sand reinforced with nonwoven geotextile loaded under triaxial compression. These conditions deviate considerably from those likely to prevail on site, where the stress regime would normally be plane strain and the soil partly saturated. Additionally, reinforcement with higher stiffness, such as geogrid, is typically used for geosynthetic-reinforced soil structures in the field. Despite these differences, the test data are expected to provide useful and insightful information for understanding the behavior and failure mechanism of reinforced earth.

ACKNOWLEDGEMENTS

The financial support for this research from the National Science Council of the Republic of China, Taiwan under grant no. NSC101-2221-E-011-112 and that from the National Taiwan University of Science and Technology under the new faculty member research funding are gratefully acknowledged. The authors also sincerely appreciate the constructive comments and feedback by the anonymous reviewers.

NOTATION

Basic SI units are given in parentheses.

A area of cross-section (m^2)
B coefficient of pore pressure (dimensionless)
C_u coefficient of uniformity (dimensionless)
C_c coefficient of gradation (dimensionless)
c' effective cohesion of soil (Pa)
c_a, c'_a anisotropic additional cohesion and the modified parameter, respectively (Pa)
COV_b coefficient of variation of bias (dimensionless)
d diameter of specimens (m)
E efficiency factor (dimensionless)
F_T resultant force of the tensile force of a reinforcement layer (N)
F_R resistant force of soil mass acting on failure surface (N)
G_s specific gravity of soil (dimensionless)
H total height of specimen, respectively (m)
h reinforcement spacing (m)
J secant stiffness of geotextile (N/m)
K_{av}, K_a, K_p and K_b lateral earth pressure coefficient, Rankin active and passive earth pressure coefficient, and coefficient of earth pressure because of the rotation of the principal stress axes within the soil mass between the geotextile layers, respectively (dimensionless)
P_{max} maximum total axial load (N)
R radius of reinforced specimen (m)
R^2 coefficient of determination (dimensionless)
r distance from the center of the geotextile disk (m).
T mobilized tensile force in geotextile (N)
$T_{L,max}$, $T_{T,max}$ maximum tensile force in longitudinal and transverse direction, respectively (N)
T_{max}, $\sum T_{max}$ maximum tensile force of reinforcement and summation of maximum tensile forces from every reinforcement layer, respectively (N)
T_{ult} ultimate tensile strength of reinforcement, respectively (N)
t', t number of pixel of deformed and undeformed reinforcement layer, respectively (dimensionless)
x, y distance from the centre of the reinforcement disks along X axis and Y axis, respectively (m)
α coefficient depending upon the effective friction mobilized along the soil–geotextile interface (dimensionless)
$\gamma_{d,min}$, $\gamma_{d,max}$ minimum and maximum dry unit weight, respectively (N/m^3)
$\Delta\sigma_1$ strength difference between reinforced and unreinforced soil (Pa)
ε tensile strain of reinforcement (dimensionless)
ε_{re} residual tensile strain of reinforcement (dimensionless)
$\varepsilon_{re\text{-}x}$, $\varepsilon_{re\text{-}y}$ measured residual tensile strain of reinforcement along X axis (transverse direction) and Y axis (longitudinal direction), respectively (dimensionless)
ε_{ult} ultimate tensile strain of reinforcement (dimensionless)
ε_1, ε_v axial strain and volumetric strain,

respectively, of specimens (dimensionless)
μ_b mean of bias (dimensionless)
σ'_1 effective axial stress (Pa)
σ'_3 effective confining pressure (Pa)
σ_d deviatoric stress (Pa)
τ interface shear stress (Pa)
ϕ', ϕ'_a effective friction angle of soil and interface friction angle between soil–geotextile interface, respectively (degree)
ψ failure plane angle (degree)

REFERENCES

Abdi, M. R., Sadrnejad, A. & Arjomand, M. A. (2009). Strength enhancement of clay by encapsulating geogrids in thin layers of sand. *Geotextiles and Geomembranes*, **27**, No. 6, 447–455.

Al-Omari, R. R., Al-Dobaissi, H. H., Nazhat, Y. N. & Al-Wadood, B. A. (1989). Shear strength of geomesh reinforced clay. *Geotextiles and Geomembranes*, **8**, No. 4, 325–336.

ASTM D4253. *Standard Test Methods for Maximum Index Density and Unit Weight of Soils Using a Vibratory Table*, ASTM International, West Conshohocken, PA, USA.

ASTM D4254. *Standard Test Methods for Minimum Index Density and Unit Weight of Soils and Calculation of Relative Density.* ASTM International, West Conshohocken, PA, USA.

ASTM D4595. *Standard Test Method for Tensile Properties of Geotextiles by the Wide-Width Strip Method*. ASTM International, West Conshohocken, PA, USA.

Athanasopoulos, G. A. (1993). Effect of particle size on the mechanical behaviour of sand–geotextile composites. *Geotextile and Geomembranes*, **12**, No. 3, 255–273.

Bathurst, R. J. & Karpurapu, R. (1993). Large-scale triaxial compression testing of geocell reinforced granular soils. *Geotechnical Testing Journal, ASTM*, **16**, No. 3, 293–303.

Boyle, S. R. (1995). Unit cell tests on reinforced cohesionless soils. *Proceedings of Geosynthetics '95, IFAI, 3*, Nashville, TN, USA, February 1995, pp. 1221–1234.

Boyle, S. R. & Holtz, R. D. (1994). Deformation characteristics of geosynthetics-reinforced soil, 1. *Proceedings of the Fifth International Conference on Geotextiles, Geomembranes and Related Products*, Singapore, September 1994, pp. 361–364.

Chandrasekaran, B., Broms, B. B. & Wong, K. S. (1989). Strength of fabric reinforced sand under axisymmetric loading. *Geotextiles and Geomembranes*, **8**, No. 4, 293–310.

Duncan, J. M. & Dunlop, P. (1968). The significance of cap and base restraint. *Journal of Soil Mechanics and Foundation, ASCE*, **94**, No. 1, 271–290.

Elias, V., Christopher, B. R. & Berg, R. R. (2001). *Mechanically Stabilized Earth Walls and Reinforced Soil Slopes Design and Construction Guidelines*, Report No. FHWA-NHI-00-043, National Highway Institute, Federal Highway Administration, Washington, DC, USA.

Farsakh, M. A., Coronel, J. & Tao, M. J. (2007). Effect of soil moisture content and dry density on cohesive soil–geosynthetic interactions using large direct shear tests. *Journal of Materials in Civil Engineering*, **19**, No. 7, 540–549.

Fabian, K. & Foure, A. (1986). Performance of geotextile-reinforced clay samples in undrained triaxial tests. *Geotextiles and Geomembranes*, **4**, No. 1, 53–63.

Gray, D. H. & Ohashi, H. (1983). Mechanics of fiber reinforcement in sand. *Journal of Geotechnical Engineering, ASCE*, **109**, No. 3, 335–353.

Gray, D. H. & Al-Refeai, T. (1986). Behavior of fabric vs. fiber-reinforced sand. *Journal of Geotechnical Engineering, ASCE*, **112**, No. 8, 804–820.

Haeri, S. M., Noorzad, R. & Oskoorouchi, A. M. (2000). Effect of geotextile reinforcement on the mechanical behavior of sand. *Geotextiles and Geomembranes*, **18**, No. 6, 385–402.

Hausmann, M. R. (1976). Strength of reinforced soil. *Proceedings of the 8th Australasian Road Research Conference*, Perth, Australia, Vol. 8, Sect. 13, pp. 1–8.

Hou, J., Zhang, M. X., Zhou, H., Javadi, A. A. & Peng, M. Y. (2011). Experiment and analysis of strength behavior of soil reinforced with horizontal-vertical inclusions. *Geosynthetics International*, **18**, No. 4, 150–158.

Ingold, T. S. & Miller, K. S. (1983). Drained axisymmetric loading of reinforced clay. *Journal of Geotechnical Engineering, ASCE*, **109**, No. 7, 883–898.

Latha, G. M. & Murthy, V. S. (2007). Effects of reinforcement form on the behavior of geosynthetic reinforced sand. *Geotextiles and Geomembranes*, **25**, No. 1, 23–32.

Leshchinsky, D., Imamoglu, B. & Meehan, C. L. (2010). Exhumed geogrid-reinforced retaining wall. *Journal of Geotechnical and Geoenvironmental Engineering, ASCE*, **136**, No. 10, 1311–1323.

Long, N. T., Guegan, Y., & Legeay, G. (1972). *Étude de la Terre Armée a l'appereil Triaxial*. Rapport de recherche No. 17, LCPC, Paris, France (in French).

Long, N. T., Legeay, G. & Madani, C. (1983). Soil-reinforcement friction in a triaxial test. *Proceedings of the 8th European Conference on Soil Mechanics and Foundation Engineering, Improvement of Ground, Helsinki*, Balkema, Rotterdam, the Netherlands, Vol. 1, pp. 381–384.

NCMA (2010). *Design Manual for Segmental Retaining Walls*, 3rd edition, Collin, J., Editor, National Concrete Masonry Association, Herndon, VA, USA.

Noorzad, R. & Mirmoradi, S. H. (2010). Laboratory evaluation of the behavior of a geotextile reinforced clay. *Geotextiles and Geomembranes*, **28**, No. 4, 386–392.

Schlosser, F. & Long, N. T. (1974). Recent results in French research on reinforced earth. *Journal of the Construction Division, Proceedings ASCE*, **100**, No. 3, 223–237.

Sridharan, A., Murthy, S., Bindumadhava, B. R. & Revansiddappa, K. (1991). Technique for using fine-grained soil in reinforced earth. *Journal of Geotechnical Engineering, ASCE*, **117**, No. 8, 1174–1190.

Tafreshi, S. N. M. & Asakereh, A. (2007). Strength evaluation of wet reinforced silty sand by triaxial test. *International Journal of Civil Engineering*, **5**, No. 4, 274–283.

Unnikrishnan, N., Rajagopal, K. & Krishnaswamy, N. R. (2002). Behaviour of reinforced clay under monotonic and cyclic loading. *Geotextiles and Geomembranes*, **20**, No. 2, 117–133.

Walters, D. L., Allen, T. M. & Bathurst, R. J. (2002). Conversion of geosynthetic strain to load using reinforcement stiffness. *Geosynthetics International*, **9**, No. 5–6, 483–523.

Wu, C. S. & Hong, Y. S. (2009). Laboratory tests on geosynthetics-encapsulated sand columns. *Geotextiles and Geomembranes*, **27**, No. 2, 107–120.

Wu, C. S. & Hong, Y. S. (2008). The behavior of a laminated reinforced granular column. *Geotextiles and Geomembranes*, **26**, No. 4, 302–316.

Zhang, M. X., Javadi, A. A. & Min, X. (2006). Triaxial tests of sand reinforced with 3D inclusions. *Geotextiles and Geomembranes*, **24**, No. 4, 201–209.

Zhang, M. X., Zhou, H., Javadi, A. A. & Wang, Z. W. (2008). Experimental and theoretical investigation of strength of soil reinforced with multi-layer horizontal-vertical orthogonal elements. *Geotextiles and Geomembranes*, **26**, No. 1, 201–209.

The Editor welcomes discussion on all papers published in Geosynthetics International. Please email your contribution to discussion@geosynthetics-international.com by 15 December 2013.